Electronic and bonding analysis of hardness in pyrite-type transition-metal pernitrides

Z. T. Y. Liu,[1] D. Gall,[2] and S. V. Khare[1,*]

[1]*Department of Physics and Astronomy, The University of Toledo, 2801 West Bancroft Street, Toledo, Ohio 43606, USA*

[2]*Department of Materials Science and Engineering, Rensselaer Polytechnic Institute, 110 8th Street, Troy, New York 12180, USA*

(Received 23 June 2014; revised manuscript received 25 August 2014; published 8 October 2014)

Most commonly known hard transition-metal nitrides crystallize in rocksalt structure (B1). The discovery of ultraincompressible pyrite-type PtN_2 10 years ago has raised a question about the cause of its exceptional mechanical properties. We answer this question by a systematic computational analysis of the pyrite-type PtN_2 and other transition-metal pernitrides (MN_2) with density functional theory. Apart from PtN_2, the three hardest phases are found among them in the 3*d* transition-metal period. They are MnN_2, CoN_2, and NiN_2, with computed Vickers hardness (H_V) values of 19.9 GPa, 16.5 GPa, and 15.7 GPa, respectively. Harder than all of these is PtN_2, with a H_V of 23.5 GPa. We found the following trends and correlations that explain the origin of hardness in these pernitrides. (a) Charge transfer from M to N controls the length of the N-N bond, resulting in a correlation with bulk modulus, dominantly by providing Coulomb repulsion between the pairing N atoms. (b) Elastic constant C_{44}, an indicator of mechanical stability and hardness is correlated with total density of states at E_F, an indicator of metallicity. (c) Often cited monotonic variation of H_V and Pugh's ratio with valence electron concentration found in rocksalt-type early transition-metal nitrides is not evident in this structure. (d) The change in M-M bond strength under a shearing strain indicated by crystal orbital Hamilton population is predictive of hardness. This is a direct connection between a specific bond and shear related mechanical properties. This panoptic view involving ionicity, metallicity, and covalency is essential to obtain a clear microscopic understanding of hardness.

DOI: 10.1103/PhysRevB.90.134102 PACS number(s): 77.84.Bw, 62.20.Qp

I. INTRODUCTION

It has been 10 years since the successful synthesis of platinum nitride by Gregoryanz *et al.* [1], followed by computational efforts to confirm its stoichiometry and structure [2–8]. After much investigation, this ultraincompressible compound, with a bulk modulus of 372 GPa [1], was finally concluded to crystallize in the pyrite structure (cubic, $Pa\bar{3}$) [9] with a stoichiometry of 1:2, thus denoted as PtN_2 [5–8]. Thereafter, the synthesis of PtN_2 spurred the endeavors in search for other noble transition-metal nitrides, among which are the experimentally synthesized OsN_2 [10], IrN_2 [6,10,11], PdN_2 [11], and very recently RhN_2 [12], four of the six so-called platinum group metal (PGM) nitrides [13]. OsN_2 and IrN_2, with Os and Ir in the same period as Pt, were confirmed to crystallize in marcasite (orthorhombic, $Pnnm$) [14–17] structure and baddeleyite (or $CoSb_2$, monoclinic, $P2_1/c$) [11,15,18] structure, respectively. PdN_2, with Pd in the same group as Pt, crystallizes in the pyrite structure [11,19] and stays metastable only above 11 GPa ambient pressure. RhN_2 has been computationally predicted [15,20] to take the marcasite structure as its possible ground state and has recently been experimentally confirmed [12].

In a conventional unit cell of this pyrite-type PtN_2, as illustrated in Fig. 1, the nitrogen atoms can be seen as two atoms: a pair taking the octahedral interstitial positions formed by metal atoms. These interstitial positions are located at the body and edge centers of the cubic cell. The relatively short distance between two adjacent nitrogen atoms (1.41∼1.42 Å), as calculated [5–7] with density functional theory (DFT) suggests the strong bonding interaction between the two nitrogen atoms, instead of them being far apart (∼2.4 Å) with weak interaction in the hypothetical fluorite structure [2]. Therefore, this interesting phase was suggested to be termed as platinum pernitride [21,22]. The calculated N-N bond length and experimental and calculated Raman spectrum showed that the N-N interaction is of a covalent, single bond nature [5–7]. In addition, all first-order Raman modes, including the high frequencies of PtN_2 come from the vibration of the N-N bond. These characteristics indicate that the extraordinary mechanical properties may be the result of the N-N bond [6]. To further illustrate its nature, Wessel and Dronskowski [21] offered a chemical point of view by means of the crystal orbital Hamilton population (COHP) analysis [23], pointing out that the surplus electrons within the antibonding $1\pi_g^*$ molecular orbital help stretch the N-N bond longer and are the source of the large bulk modulus.

Although the space groups of these newly discovered PGM nitrides are different, they have a lot in common: (a) N-N interaction exists in the cell with an interatomic length corresponding to a single bond formation; (b) nitrogen atoms form octahedra to coordinate the metal atoms [15,21]; (c) one phase can transform to another by orientation changes of the N-N bond or a small distortion of the structure [15,21]. Therefore, although most of them do not favor the pyrite structure as their ambient pressure ground state, one can nevertheless extract abundant information by doing a systematic study for a large class of transition-metal elements in the periodic table. Various studies have been carried out for pyrite-type pernitrides of 5*d* transition metals on structure and energetics [24], on elastic constants and electronic states [25], and more focused on noble transition metals [26].

In the following sections of this paper, we report our analysis on the trends and correlations of 20 different 3*d* and 4*d* transition-metal pernitrides in the pyrite structure. We report their cohesive energy with comparison to the fluorite-type counterparts, structural parameters such as lattice constant,

*sanjay.khare@utoledo.edu

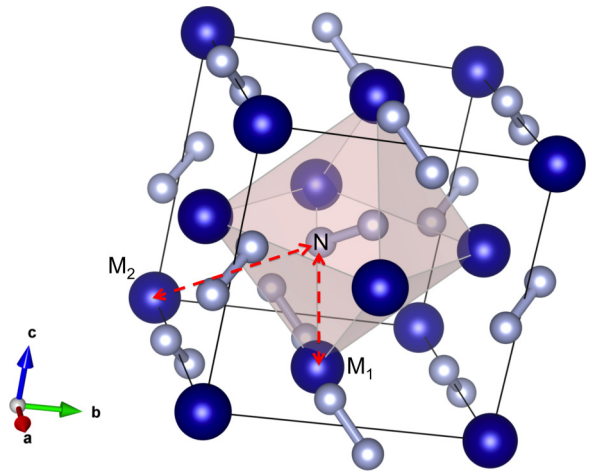

FIG. 1. (Color online) The conventional unit cell of pyrite-type ($Pa\bar{3}$) [9] transition-metal pernitrides. The dark blue spheres represent metal atoms at Wyckoff position 4*a* (corners and face centers), and silver spheres represent nitrogen atoms at Wyckoff position 8*c*. The nitrogen atoms can be alternatively seen as two atoms, a pair taking the metal octahedron interstitial Wyckoff positions 4*b* (body and edge centers). M_1 is the closest coordinating metal atom for a nitrogen atom (N), and M_2 is the closest in the [111] direction.

internal parameter and bond lengths, elastic constants and mechanical properties, Bader charge transfer, and electronic density of states (DOS). Finally, we show the relation of mechanical properties to the bonding characteristics of an atom with its neighboring atoms, namely *M*-*M*, *M*-N, and N-N, in the scheme of projected COHP (pCOHP) analysis [23,27–29]. Also, from our calculation of the 5*d* metal pernitrides, there are only three mechanically stable phases: HfN_2, IrN_2, and PtN_2. Of these, only PtN_2, exhibiting high hardness, is further analyzed comprehensively.

We found significant variations in the mechanical properties of these materials, especially among their shear modulus, Pugh's ratio, and hardness. Previous studies have proposed electronic indicators, or controlling factors, such as valence electron concentration (VEC) [30–33] and ionicity [34] for determining extreme values in such mechanical properties. We found two new parameters in these pyrite-type phases. One of these is the total density of electronic states at the Fermi energy, directly correlated with metallicity, and the other is the change in *M*-*M* bond strength under a shearing strain. Both of them show predictive potential for determining extreme elastic and mechanical properties.

II. COMPUTATIONAL METHODS

We performed our calculations with the Vienna *Ab initio* Simulation Package (VASP) [35–38], implementing DFT to solve the Kohn-Sham equations [39,40]. The one-electron orbitals and the electronic charge density are expanded in plane wave basis sets. We chose potentials using the projector-augmented wave (PAW) [41,42] method under PW91 general gradient approximation (GGA) [43,44]. We selected the following PAW potentials of transition-metal elements—Sc_sv, Ti_pv, V, Cr, Mn, Fe, Co, Ni, Cu, Zn for the 3*d* row and Y_sv, Zr_sv, Nb_pv, Mo_pv, Tc_pv, Ru, Rh, Pd, Ag, Cd for the 4*d* row—to ensure quality, per Ref. [45]. Kinetic energy cutoff value was chosen to be 400 eV for all phases. Monkhorst-Pack k-point mesh [46,47] was used at 11 × 11 × 11 density with the inclusion of Γ point. Tests with a higher energy cutoff and a denser mesh showed that our chosen values were enough to converge the total energy below a difference of ±1 meV. For the electronic minimization, Methfessel-Paxton order 1 smearing method was used and a convergence criterion was set at 10^{-5} eV/atom. For ionic relaxation to obtain pyrite structure's internal parameter, and pushing ions into their respective equilibrium positions when under strain, we employed conjugate-gradient algorithm and a force criterion of 0.01 eV/Å. For each species, we enabled spin polarization in all calculations.

A. Methods for structural and mechanical properties

In order to determine the equilibrium lattice constant (a), we did a series of runs for each phase, varying the lattice constant in a range of 1 Å around the estimated energy minimum configuration. This total energy versus volume data was fitted to the form of Birch-Murnaghan [48,49] equation of state as formulated by Zhao *et al.* [50]. During each run, ions were allowed to fully relax within the symmetry constraints of space group $Pa\bar{3}$, while the cell shape and volume were fixed. From the fits, the equilibrium lattice constant and bulk modulus (B) were extracted. Further fitting refinement showed discrepancies of lattice constant below 0.005 Å. Then, with the equilibrium lattice constant and the relaxed ionic positions of the run closest to the equilibrium point from above, we relaxed the ions again while keeping the cell shape and volume fixed to obtain the precise value of internal parameter (x) at Wyckoff position 8*c* [9] of the pyrite structure and the total energy per formula unit (E_{MN_2}) of this minimum configuration.

We also calculated the total energy of the spin-polarized single atom of the transition metal (E_M) and nitrogen (E_N) in a large supercell with a side of 12 Å. We computed the cohesive energy per atom (E_{coh}) as $E_{coh} = (E_M + 2E_N - E_{MN_2})/3$, which yields the thermodynamic stability of the compound.

To compute the three independent elastic constants C_{11}, C_{12}, and C_{44} of these cubic phases, we applied two sets of strains to the unit cell following the forms of Eq. (11) and Eq. (13) by Mehl *et al.* [51]. For each set, we strained the unit cell to different values below 5% and fit the output total energy data points to a second-order polynomial to acquire the coefficients of the fit. The coefficients so obtained yield values of C_{11}–C_{12} and ½ C_{44}. The bulk modulus B equals $(C_{11} + 2C_{12})/3$. The two coefficients, along with the value of B obtained earlier, were used to solve for the three elastic constants. In all the strained computations, ions were allowed to relax to their equilibrium positions.

Crystals have to satisfy a set of constraints on elastic constants in order to be mechanically stable. For cubic structures, they are $C_{11} > |C_{12}|$, $C_{11} + 2C_{12} > 0$, and $C_{44} > 0$ [52]. The mechanical properties of the stable phases, including shear modulus (G), Pugh's ratio (k), and Vicker's hardness (H_V) formulated by Chen *et al.* [53] and Tian *et al.* [54], can be derived from the elastic constants as shown earlier [55–57]. In this paper, we used the formulation of Tian *et al.* [54], $H_V = 0.92\, k^{1.137} G^{0.708}$.

TABLE I. Comparison with other calculated and experimental values of pyrite-type PtN_2. Mechanically stable pyrite-type 5*d* phases and fluorite-type 3*d* and 4*d* phases are also included. Listed values are equilibrium lattice constant (a), internal parameter (x) of $Pa\bar{3}$ Wyckoff position 8*c* [9], elastic constants C_{11}, C_{12}, C_{44}, and bulk modulus (B).

	a (Å)	x	C_{11} (GPa)	C_{12} (GPa)	C_{44} (GPa)	B (GPa)
PtN_2 (this paper)	4.877	0.416	661.9	69.3	128.8	266.9
PtN_2 LAPW-GGA[a]	4.862	0.415	668	78	133	272
PtN_2 PP-PW91[b]	4.877	0.417	713	90	136	298
PtN_2 PP-PBE[c]	4.848	0.415	696	83	136	288
PtN_2 PAW-PW91[d]	4.875					278
PtN_2, Exp.[e]	4.804					372
pyrite-HfN_2	5.129	0.415	359.4	171.9	124.7	234.4
pyrite-IrN_2	4.858	0.418	691.9	97.8	67.5	295.9
fluorite-TcN_2	4.892		314.9	283.8	31.1	294.2
fluorite-RuN_2	4.867		320.6	283.4	37.1	295.8
fluorite-RhN_2	4.886		291.0	261.8	29.2	271.6
fluorite-PdN_2	4.979		254.1	200.4	53.7	218.3
fluorite-AgN_2	5.155		191.7	156.0	35.6	167.9

[a]Yu *et al.* [7].
[b]Gou *et al.*, [8].
[c]Young *et al.* [5].
[d]Crowhurst *et al.* [6].
[e]Gregoryanz *et al.* [1].

B. Methods for electronic properties and bonding characteristics

Bader charge transfer [58,59] analysis was done with the implementation of Henkelman *et al.* [60,61], Sanville *et al.* [62], and Tang *et al.* [63], following the guidelines in Ref. [64]. The fast Fourier transform (FFT) grid for charges (the second FFT grid) was set at 250 × 250 × 250. The total electronic DOS were calculated using the tetrahedron method with Blöchl corrections [65] and a 21 × 21 × 21 k-point mesh.

To quantify the covalent and metallic nature of bonding, we projected plane waves to local orbital basis functions to extract COHP [23]. This projection was achieved by using the program Local-Orbital Basis Suite Towards Electronic-Structure Reconstruction (LOBSTER) [27–29]. The COHP approach is a more relevant concept [23] for application in first-principles DFT computations compared to the more well-known crystal orbital overlap population (COOP) [66,67] in solid-state chemistry. It is able to partition band-structure energy into orbital-pair contributions and generate energy-resolved plots [23], therefore revealing the bonding, nonbonding, and antibonding interaction between two chosen atoms, offering a more detailed view of electronic structure. The integration of COHP for all energies up to E_F gives integrated COHP (ICOHP) to render a quasiquantitative interpretation [27] of the net bonding characteristics. Some care in interpretation is needed since negative values of the COHP suggest bonding contribution, opposite to the sign convention with COOP. Therefore, we followed the convention in Refs. [27,28] to directly provide −COHP for the ease of comprehension. The wave-function output from VASP was expressed as plane waves that were projected into local orbitals by LOBSTER. Hence, our results will be named per convention as pCOHP and its integral as IpCOHP [27,28] in this paper.

The LOBSTER manual [29] offers detailed instructions to carry out an analysis with the output files of one VASP static run. Apart from following them closely, we accelerated the last VASP calculation step that requires a full (not symmetry reduced) k-point mesh by using a charge density file from the previous self-consistent run. Sample calculations suggested this approach yielded the same results. Although it is suggested a denser than usual k-point mesh is not necessary [27], we nevertheless used a denser one (17 × 17 × 17) in the last VASP run because most phases we studied in this paper were metallic. We let LOBSTER output the IpCOHP of all the atom pairs and averaged the ones that are symmetry-equivalent in terms of their atomic positions. For each phase, we did one analysis for the cell at equilibrium and another under a 10% C_{44} [110]-oriented shearing strain, which may reveal the nature of mechanical properties, as suggested by Sangiovanni *et al.* [32,33]. All atoms are allowed to relax following the guidelines detailed above.

III. RESULTS AND DISCUSSION

Table I lists the structural and elastic parameters for PtN_2 calculated in this paper and a comparison with other calculated and experimental values. Our results closely match other computations and experimental measurements for PtN_2 [1,5–8]. For other 3*d* and 4*d* pernitrides, no such comparison is available. We note that the underestimation of bulk modulus calculated with GGA is a well-known effect [68,69], and it does not hinder the purpose of this paper. If we obtain values of a phase suggesting high hardness, it can only be harder in reality if the phase can be synthesized and remain thermodynamically stable.

A. Energetic properties

Figure 2 shows the cohesive energy per atom of the 20 pyrite-type, 3*d*, and 4*d* transition-metal pernitrides. Precise values are listed in Table II. For comparison, we also included

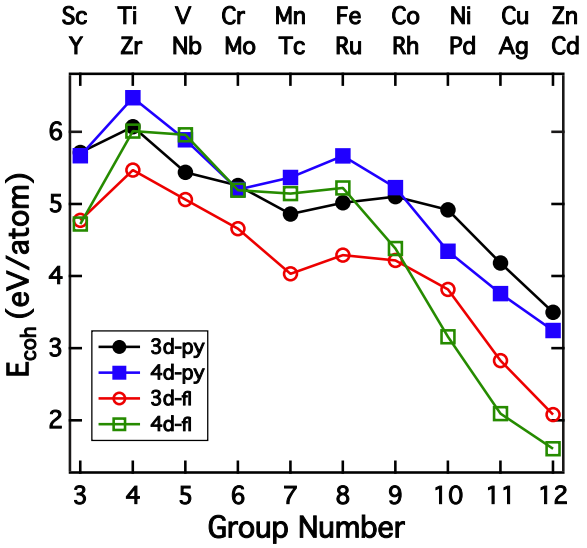

FIG. 2. (Color online) Cohesive energy per atom (E_{coh}) of the transition-metal pernitrides versus the group number of their corresponding metals. Circles correspond to metals from the 3*d* row and squares to those from the 4*d* row. Filled symbols depict the pyrite (py) structure and unfilled symbols the fluorite (fl) structure.

our computed values of the corresponding fluorite-type phases. From the figure, we observe that in most cases the E_{coh} value of the pyrite-type phase is larger than that of the fluorite-type phase. This indicates that thermodynamically pyrite-type phases are relatively more stable. For the cases of NbN_2 and MoN_2, the two structures have comparable values. However, despite these few similarities in E_{coh}, further elastic constant calculations show that fluorite-type phases are mostly mechanically unstable or very soft (estimated $H_V < 2$ GPa). The only five mechanically stable fluorite-type phases are the nitrides of Tc, Ru, Rh, Pd, and Ag, all in the 4*d* row. Their computed structural and elastic parameters are listed in Table I. Since there is no current experimentally synthesized transition-metal nitride in this structure, we do not further analyze them.

B. Structural properties

In Table II lattice constant (a), internal parameter (x), and the Bader charge transfer (q_{trans}) from a transition-metal atom

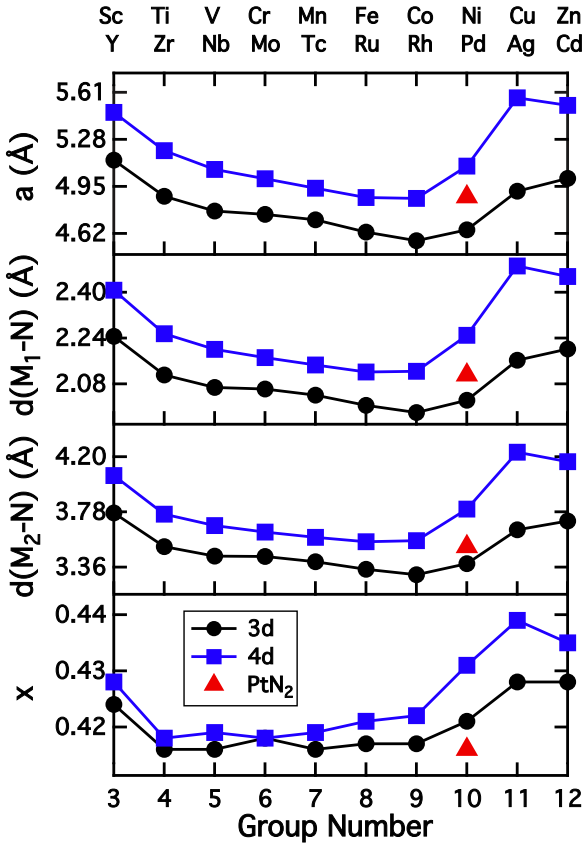

FIG. 3. (Color online) Equilibrium lattice constant (a), distance $d(M_1\text{-N})$ between M_1 and N, distance $d(M_2\text{-N})$ between M_2 and N, and internal parameter (x) of Wyckoff position 8*c* [9] of the pyrite-type transition-metal pernitrides versus the group number of their corresponding metals. The pernitrides corresponding to metals from the 3*d* and 4*d* rows are represented by black circles and blue squares. Red triangles represent pyrite-type PtN_2 shown for comparison.

to the nitrogen atoms are listed. To connect these values to physical bonding between different atoms, we utilized the notations for atoms illustrated in Fig. 1. In this notation we computed the distance between one nitrogen atom (N) and its closest nitrogen atom $d(\text{N-N}) = \sqrt{3}a\,(1-2x)$, its closest metal atom $d(M_1\text{-N}) = a\sqrt{x^2 + 2(0.5-x)^2}$, and its adjacent metal atom in the [111] direction $d(M_2\text{-N}) = \sqrt{3}ax$. Figure 3

TABLE II. Equilibrium lattice constant (a), internal parameter (x) of Wyckoff position 8*c* [9], cohesive energy per atom (E_{coh}), and Bader charge transfer (q_{trans}) from a metal atom to nitrogen atoms of the pyrite-type transition-metal pernitrides, MN_2.

Group of *M*	*M*		*a* (Å)		*x*		E_{coh} (eV/atom)		q_{trans} (*e*)	
3	Sc	Y	5.134	5.469	0.424	0.428	5.71	5.67	1.83	1.96
4	Ti	Zr	4.881	5.201	0.416	0.418	6.07	6.47	1.98	2.31
5	V	Nb	4.777	5.069	0.416	0.419	5.44	5.89	1.63	2.05
6	Cr	Mo	4.754	5.004	0.418	0.418	5.26	5.20	1.46	1.76
7	Mn	Tc	4.716	4.938	0.416	0.419	4.86	5.37	1.44	1.51
8	Fe	Ru	4.630	4.872	0.417	0.421	5.02	5.67	1.23	1.11
9	Co	Rh	4.569	4.866	0.417	0.422	5.10	5.23	1.03	0.91
10	Ni	Pd	4.645	5.093	0.421	0.431	4.92	4.34	0.97	0.69
11	Cu	Ag	4.916	5.572	0.428	0.439	4.18	3.76	0.85	0.59
12	Zn	Cd	5.007	5.519	0.428	0.435	3.50	3.25	1.07	0.96

TABLE III. Elastic constants C_{11}, C_{12}, C_{11}-C_{12}, C_{44} and mechanical stability of the pyrite-type transition-metal pernitrides, MN_2. Mechanically stable phases are denoted as "S" and unstable ones as "U."

Group of M	M		C_{11} (GPa)		C_{12} (GPa)		C_{11} - C_{12} (GPa)		C_{44} (GPa)		Mechanical stability	
3	Sc	Y	129.0	24.4	161.7	185.2	− 32.7	− 160.8	61.6	56.0	U	U
4	Ti	Zr	354.7	286.1	149.7	178.5	205.0	107.6	97.9	98.5	S	S
5	V	Nb	391.0	302.6	137.3	213.2	253.7	89.3	9.4	− 38.4	S	U
6	Cr	Mo	392.5	386.4	104.8	145.2	287.7	241.3	61.4	− 20.0	S	U
7	Mn	Tc	421.2	471.5	60.7	120.1	360.5	351.4	104.7	24.3	S	S
8	Fe	Ru	466.2	510.5	46.8	113.0	419.4	397.5	30.7	− 52.7	S	U
9	Co	Rh	518.4	500.4	63.9	71.8	454.6	428.6	89.1	52.7	S	S
10	Ni	Pd	338.4	142.2	64.3	38.2	274.0	104.0	86.7	33.9	S	S
11	Cu	Ag	66.8	36.6	91.3	31.6	− 24.5	5.0	29.2	12.0	U	S
12	Zn	Cd	157.7	93.1	45.3	7.2	112.4	85.9	57.7	14.2	S	S

illustrates the close correlation between a, $d(M_1\text{-N})$, $d(M_2\text{-N})$, and x that is found as the group number of the metal atom (M) varies. This correlation shows that as the M atom changes, these four quantities change at a similar rate.

C. Mechanical properties

Table III lists the three independent elastic constants, C_{11}, C_{12}, C_{44}, and C_{11}–C_{12}, for convenience of checking the mechanical stability criteria. Out of the 20 pyrite-type phases of 3d and 4d transition metals, we observe six mechanically unstable ones, namely ScN_2 and CuN_2 in the 3d row, and YN_2, NbN_2, MoN_2, and RuN_2 in the 4d row. Apart from PtN_2, the values for the other two mechanically stable 5d phases, HfN_2 and IrN_2, are provided in Table I as well.

Table IV shows the derived results for mechanical properties, including bulk modulus (B), shear modulus (G), Pugh's ratio (k), and Vickers hardness (H_V), using the methods described in Sec. II. Figure 4 shows the trends in values as the group number of the metal atom changes. Notable hard phases are observed in the 3d row, namely MnN_2 (H_V = 19.9 GPa), CoN_2 (16.5 GPa), and NiN_2 (15.7 GPa). In the 5d period, the H_V values for the three mechanically stable phases, HfN_2, IrN_2, and PtN_2, are 11.1 GPa, 11.1 GPa, and 23.5 GPa, respectively. These compare well with the computed hardness values for other typical hard coating materials, rocksalt-type TiN (24.0 GPa) and VN (14.0 GPa) from Ref. [56], which matched well with experimental measurements.

D. Bader charge transfer and N-N bond

Figure 5 shows a correlation between the structural parameter d(N-N) and Bader charge transfer (q_{trans}). [1]. This is a different pattern from the one found in Fig. 3 for the other structural parameters. This correlation in Fig. 5 may be qualitatively explained in two ways. When more charges are transferred from M to N, (a) the Coulomb repulsion between the two similarly charged N atoms will have an elongating impact on the N-N bond and (b) following Wessel and Dronskowski's reasoning [21], when more charges are transferred to the nitrogen dimer, more antibonding states are filled and hence the N-N bond becomes longer. This effect can be visually observed in Fig. 6, which depicts color contour plots of the charge density distribution of four selected phases in the $(1\bar{1}0)$ plane passing through the origin [0,0,0] of the unit cell shown in Fig. 1. They are phases of 3d transition metals VN_2 (Group 5), MnN_2 (Group 7), FeN_2 (Group 8), and 4d, TcN_2 (Group 7), respectively. The reason to choose these four phases is that, as demonstrated in Fig. 4, they exhibit very large variations in mechanical properties, although lying close together in the periodic table. We can clearly see that as the transition-metal element moves from V through Mn to Fe, as q_{trans} from 1.63 e through 1.44 e to 1.23 e, and as d(N-N) from

[1]We note that the values of q_{trans} describe the charge transfer from a metal atom to two nitrogen atoms, so each nitrogen atom gets half of it.

TABLE IV. Bulk modulus (B), shear modulus (G), Pugh's ratio (k), and Vickers hardness (H_V) of the pyrite-type transition-metal pernitrides, MN_2. Mechanically unstable phases are denoted as "U."

Group of M	M		B (GPa)		G (GPa)		k		H_V (GPa)	
3	Sc	Y	U	U	U	U	U	U	U	U
4	Ti	Zr	218.0	214.3	99.7	77.3	0.46	0.36	9.8	6.3
5	V	Nb	221.9	U	35.6	U	0.16	U	1.4	U
6	Cr	Mo	200.7	U	87.0	U	0.43	U	8.4	U
7	Mn	Tc	180.9	237.2	130.4	61.0	0.72	0.26	19.9	3.6
8	Fe	Ru	186.6	U	74.5	U	0.40	U	6.8	U
9	Co	Rh	215.4	214.6	131.1	96.4	0.61	0.45	16.5	9.4
10	Ni	Pd	155.7	72.8	104.3	40.3	0.67	0.55	15.7	6.4
11	Cu	Ag	U	33.3	U	6.5	U	0.19	U	0.5
12	Zn	Cd	82.8	35.8	57.1	22.6	0.69	0.63	10.6	4.9

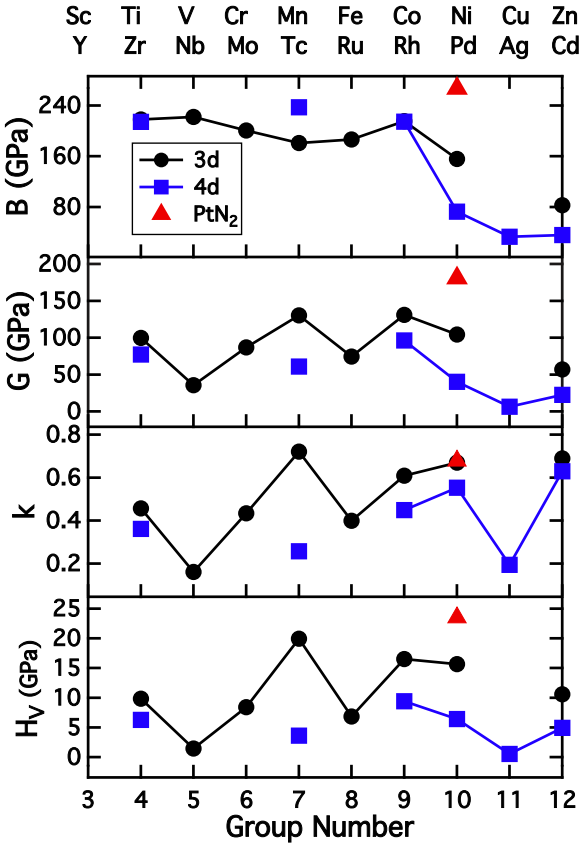

FIG. 4. (Color online) Bulk modulus (B), shear modulus (G), Pugh's ratio (k), and Vickers hardness (H_V) of the pyrite-type transition-metal pernitrides versus the group number of their corresponding metals. The pernitrides corresponding to metals from the 3d and 4d rows are represented by black circles and blue squares. Red triangles represent pyrite-type PtN_2 shown for comparison. The lines are a guide to the eye. Missing symbols correspond to mechanically unstable phases in Table IV.

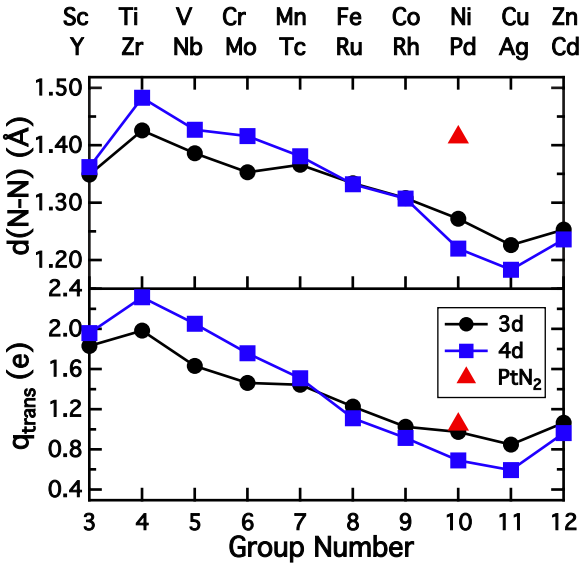

FIG. 5. (Color online) Distance d(N-N) between two bonding nitrogen atoms and Bader charge transfer (q_{trans}) from a metal atom to nitrogen atoms of the pyrite-type transition-metal pernitrides versus the group number of their corresponding metals. The pernitrides corresponding to metals from the 3d and 4d rows are represented by black circles and blue squares. Red triangles represent pyrite-type PtN_2 shown for comparison. Since the two nitrogen atoms are in equivalent positions, they split the charges equally.

1.386 Å through 1.366 Å to 1.334 Å, there is a higher and higher charge density lying between the two nitrogen atoms, strengthening the N-N covalent bond because the Coulomb repulsion between them gets weaker. Similar observation can be made if one compares MnN_2 and TcN_2, whose transition metals belong to the same group but a different period. TcN_2 has a slightly larger value of q_{trans} (1.51 e) than that of MnN_2 (1.44 e), and a larger value of d(N-N) (1.381 Å) than that of MnN_2 (1.366 Å); accordingly, it has less charge density in between the two nitrogen atoms.

Another observable effect in Fig. 6 is that following the same sequence, from V through Mn to Fe in the 3d period, there is a higher and higher charge density between the nitrogen atom and its closest transition-metal atom. This suggests the interaction between the two elements in the pyrite structure moves from being dominantly ionic to being more covalent, in agreement with what we see from the decreasing q_{trans} pattern in Fig. 5.

A mild correlation between q_{trans} and B in Fig. 4 is observed. This correlation is used by Wessel and Dronskowski [21] to explain the extraordinarily high value of B (our calculation: 266.9 GPa) for pyrite-type PtN_2. We clarify this further by noting that this correlation between q_{trans} and B in pyrite-type 3d and 4d transition-metal pernitrides is influenced dominantly by Coulomb repulsion. As mentioned earlier, charge transfer exerts its influence on the N-N bond length in two ways, Coulomb repulsion and antibonding state filling, which jointly lead to the elongation of N-N bond. For PtN_2, in Fig. 5 we notice the value of d(N-N) is larger than

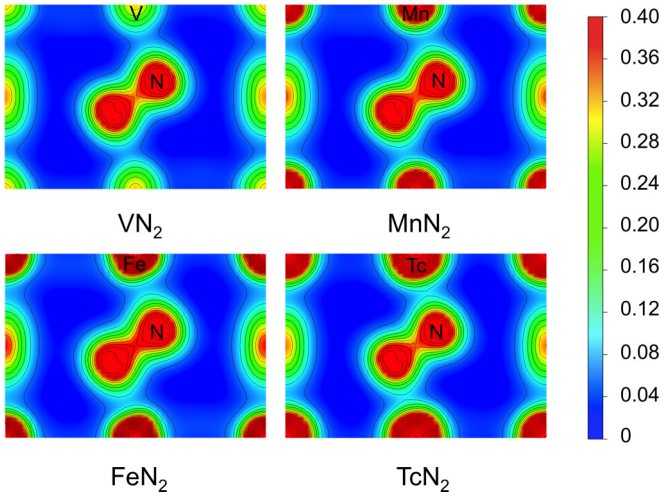

FIG. 6. (Color online) Electronic charge density distribution on the $(1\bar{1}0)$ plane passing through point [0,0,0] of pyrite-type 3d transition-metal pernitrides VN_2 (Group 5), MnN_2 (Group 7), FeN_2 (Group 8), and 4d transition-metal pernitride TcN_2 (Group 7). The color scale is shown by the unit of eÅ^{-3}. Values larger than 0.4 are represented in red.

TABLE V. Inverted integrated projected crystal orbital Hamilton population (−IpCOHP) of the closest M-M, M-N, and N-N bonds of the pyrite-type transition-metal pernitrides, MN_2. Listed are the averaged values of equivalent pairs in a cell. The three columns to the right are the changes in values (δ) when a 10% C_{44} [110]-oriented shearing strain is applied to the conventional unit cell.

		−IpCOHP (meV)					
Group of M	M of MN_2	M-M	M-N	N-N	δ (M-M)	δ (M-N)	δ (N-N)
4	Ti	−2.4	1908.1	5456.0	29.3	−25.9	237.1
	Ti (strained)	26.8	1882.2	5693.1			
5	V	492.8	1654.6	3205.6	42.0	−16.9	45.3
	V (strained)	534.8	1637.7	3250.9			
6	Cr	359.2	1604.4	4051.2	20.6	−12.1	9.3
	Cr (strained)	379.8	1592.2	4060.6			
7	Mn	414.6	1559.8	3502.7	18.6	−11.9	58.2
	Mn (strained)	433.2	1547.8	3560.8			
8	Fe	486.1	1530.1	3730.2	30.2	−9.1	55.5
	Fe (strained)	516.3	1521.0	3785.7			
9	Co	121.7	1802.8	7837.0	25.2	−9.3	69.7
	Co (strained)	146.9	1793.5	7906.7			
10	Ni	82.9	1537.2	8755.5	14.8	−19.4	110.6
	Ni (strained)	97.7	1517.8	8866.0			
12	Zn	−73.3	1095.1	8479.4	9.0	−9.6	65.1
	Zn (strained)	-64.3	1085.5	8544.5			
7 (4d)	Tc	477.4	1754.8	3231.7	48.7	−25.4	195.1
	Tc (strained)	526.1	1729.3	3426.8			
10 (5d)	Pt	−191.3	2391.5	6544.4	−11.2	−23.5	109.6
	Pt (strained)	−202.5	2368.0	6653.9			

those of most 3d and 4d transition-metal pernitride phases despite the similarity in q_{trans}. This clearly indicates that the contribution from antibonding state filling is needed to explain its larger d(N-N). On the other hand, we examined all −pCOHP versus energy plots of the compounds listed in Table V. Unlike the case of PtN_2 and BaN_2 analyzed by Wessel and Dronskowski [21], we did not observe any predictable shift or less filling of the antibonding states in the region directly below E_F. Therefore, we conclude that this correlation between q_{trans} and B in these pernitrides, compared with PtN_2, is controlled dominantly by Coulomb repulsion.

Note that Group 7 transition-metal pernitrides MnN_2 and TcN_2 have very different values of G, k, and H_V in Fig. 4, although their q_{trans} and charge density distribution patterns are very similar in Figs. 5 and 6. In addition to this, as the transition metal (M) moves from the early to late region in the period, the electronegativity difference between M and N becomes smaller; therefore, charge transfer from M to N becomes smaller. One might be tempted to conclude that accompanying this smaller charge transfer would be a decrease in metallicity, leading to a decrease in G, k, or H_V. This reasoning holds true for the early transition-metal carbides and nitrides in Ref. [34]. However, in the pyrite structure analyzed here, although we do observe the decrease in ionic contribution, the material's ductility does not necessarily always increase, as seen from Fig. 4. Ductility is a shear related mechanical property, and it is associated with C_{44} and DOS at Fermi energy, an indicator of metallic contribution analyzed later in Sect. IIIE and Fig. 8. To conclude, ionicity within a solid is not a major decisive factor on its shear related behavior, such as ductility and hardness, for pyrite-type transition-metal nitrides.

E. Electronic DOS

We now turn our attention to a more detailed analysis of the electronic structure of these 20 phases. Figure 7 shows the total DOS for the 3d pernitrides. For each phase, spin up states and spin down states are added together. We observe the gradual shift of the peaks in the DOS to a deeper energy region as more and more valence electrons are included in the system, one per step to the right in the 3d row. The 10 phases in the 4d row, though not shown here, behave similarly. In Fig. 8, we focus on the correlation between the total DOS at the Fermi energy (E_F) and the elastic constant combinations that heavily influence mechanical stability and mechanical properties, C_{11}–C_{12} and C_{44}. Again spin polarization is taken into consideration, and the values in the corresponding panels are added-up results. In order to avoid numerical imprecision, we in effect integrated the total DOS in a small window around E_F from $E_F - 0.2$ eV to $E_F + 0.2$ eV to obtain the number of electronic states per unit cell. We see C_{11}–C_{12} does not have a clear correlation with total DOS at E_F, but C_{44} demonstrates very satisfactory anticorrelation, especially in the same row. A reasonable explanation of this anticorrelation is that as the total DOS at E_F increases, covalent/ionic behavior gradually transforms into metallic behavior, thus turning the hard and brittle phase, characterized by a covalent bonding network and/or ionic interaction, into a soft and ductile metallike phase, characterized by delocalized electrons at E_F and stronger M-M interactions. Such an anticorrelation has also been seen for 3d transition-metal nitrides in zincblende, rocksalt, and cesium chloride structures [56], and 3d, 4d, 5d transition-metal nitrides in NbO structure [55], and can serve as an indicator to screen a very large number of compounds in search of extraordinary hardness, without calculating all the

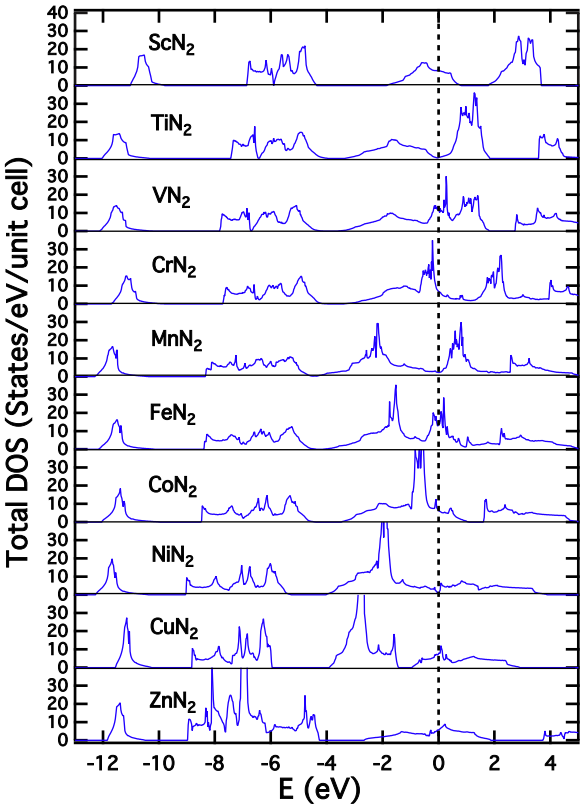

FIG. 7. (Color online) Total DOS per unit cell of the 10 3*d* pyrite-type transition-metal pernitrides. Fermi energy is set to zero in each panel.

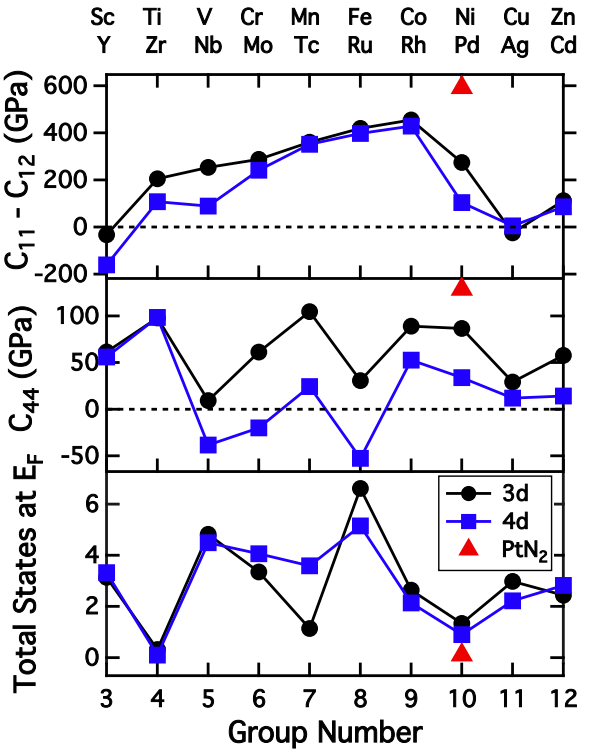

FIG. 8. (Color online) Elastic constant C_{11}–C_{12}, C_{44}, and the number of electronic states per unit cell in a narrow window around E_F (from $E_F - 0.2$ eV to $E_F + 0.2$ eV) of the pyrite-type transition-metal pernitrides versus the group number of their corresponding metals. The pernitrides corresponding to metals from the 3*d* and 4*d* rows are depicted by black circles and blue squares. Red triangles represent pyrite-type PtN_2 shown for comparison. Notice the anticorrelation between C_{44} and total states at E_F.

elastic constants, which is computationally expensive. This anticorrelation is also well observed in experimental data of early transition-metal nitrides and carbides [34]. In those cases, ionic bonds become weaker and metallic bonds stronger with a higher DOS at E_F as the transition metal moves from Group 4 to Group 6.

Following the remarks in Sec. IIID, one might also be tempted to think that as the transition metal (M) moves from the early to the late region, extra electrons are added into the system, increasing VEC, thus increasing the overall metallicity and further increasing the ductility of the material. This rule has been true for rocksalt-type nitrides of early transition metals from Group 4 to Group 6 [32,33,70]. However, the trends of G, k, and H_V in Fig. 4 show that it is not quite applicable to other structures such as the pyrite-type in this study or other previously explored structures [55–57]. From Figs. 7 and 8, we do not see that the total DOS at E_F keeps increasing. Rather, it could land on more than one low DOS region, including pernitride cases such as MnN_2, CoN_2, and NiN_2, resulting in an increase in shear related mechanical properties. It is especially the case of PtN_2, where its E_F moves into a band gap, as can be seen in Fig. 9, makes itself a semiconductor, and results in mechanical stability and exceptional hardness. For comparison, in the DOS patterns of IrN_2 and AuN_2 (mechanically unstable), the two adjacent 5*d* phases to PtN_2, E_F land on the left and right side of the gap, respectively, demonstrating metallicity. This is seen in Fig. A in the Supplemental Material [71]. In general, the

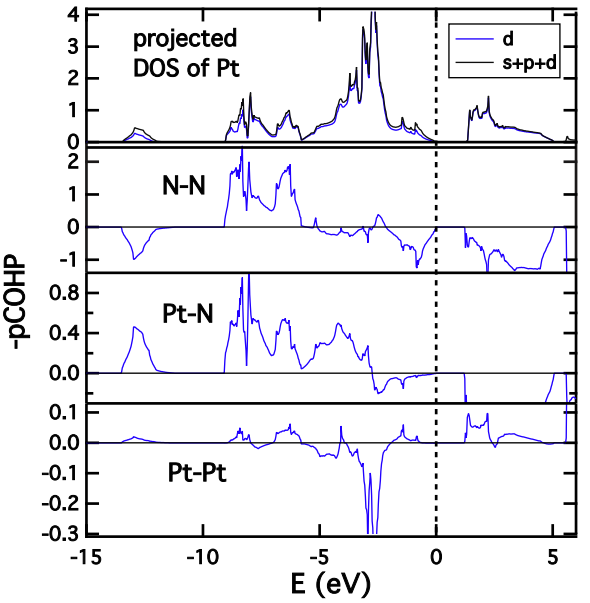

FIG. 9. (Color online) Top panel is the projected DOS of Pt in PtN_2. The −pCOHP of bonds N-N, Pt-N, and Pt-Pt in the cell of pyrite-type PtN_2 is shown in the bottom three panels. Positive and negative values indicate bonding and antibonding contributions, respectively. Fermi energy is set to zero in each panel.

optimal VEC that leads to minimal metallicity depends strongly on the structure, the nature of bonding, and the different roles electrons play in the bonding picture, and there could be more than one optimal VEC along the transition-metal period. The importance of systematic analyses lies in obtaining such information and shedding light on the bonding nature in specific cases leading to more general principles.

F. Projected COHP and *M*-*M* bond

In Fig. 9, we plotted the locally projected DOS of Pt and the −pCOHP of N-N, Pt-N, and Pt-Pt. We also reproduced, although not shown here, the five examples, i.e., bulk diamond, bulk GaAs, bulk Ti, carbon nanotube, and C_{60} in Ref. [28] to a very high precision. The patterns of Pt-N and N-N are consistent with previous tight-binding linear muffin-tin orbital atomic-sphere approximation (TB-LMTO-ASA) calculations [21]. A discernible difference is that right below E_F, for the Pt-N bond there is a small negative region in our projected plane wave calculation, whereas TB-LMTO-ASA gives a positive region. We also did the same calculation with PAW-local density approximation (LDA) potentials, but the negative region remained.

We did the same pCOHP analyses for a large number of mechanically stable phases, namely pyrite-type nitrides with 3*d* metals, TiN_2, VN_2, CrN_2, MnN_2, FeN_2, CoN_2, NiN_2, ZnN_2, additionally TcN_2 with a 4*d* metal, and PtN_2 with a 5*d* metal. Due to the relative expensive nature of such calculations, we did not include all other 4*d* metal phases. In Table V, we list the integrated values of −pCOHP up to E_F for all three neighboring atom pairs of these phases and the changes to them, i.e., δ(−IpCOHP), when a 10% C_{44} [110]-oriented shearing strain is applied. We aim to find out the possible correlations of these trends with those of elastic or mechanical properties. The absolute values of −IpCOHP of these different compounds are not particularly informative for our interest, but the changes in them under strain turn out to be quite indicative. After all, they share the very similar pyrite structure, and by monitoring the change with strain we rule out the intrinsic differences in their absolute values that are not comparable between phases with different transition-metal elements.

We observe a mild anticorrelation between C_{44}, G, and H_V and δ(−IpCOHP) of the *M*-*M* bond in Table V. The case for Pugh's ratio (k) is even more obvious. These physical quantities reflect a similar aspect of the material—shear related mechanical properties. In Fig. 10, we compare the values of δ(−IpCOHP) for N-N, *M*-N, and *M*-*M* bonds to k as a function of the group number of the metal atoms. It is quite remarkable to notice the anticorrelation between δ(−IpCOHP) of *M*-*M* and k, an indicator for brittleness. These observations from Fig. 10 that are true for pyrite-type transition-metal pernitrides suggest the following conjecture: The more −IpCOHP of the *M*-*M* bond increases its value under the same shearing strain applied to a collection of phases in the same structure, the less brittle the phase is and the softer it is likely to be. It is reasonable to make this statement because physically a stronger positive *M*-*M* bond response to shearing strain indicates more metallicity. A similar observation can be made with the ICOOP data in Refs. [32,33] by Sangiovanni *et al.* on rocksalt-type Ti and V nitrides when alloyed with Al, Nb, Ta, Mo, or W nitrides.

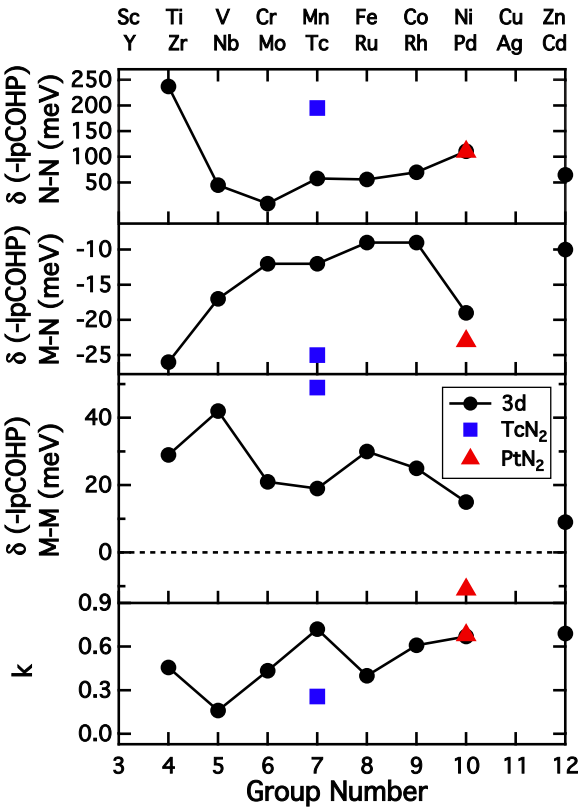

FIG. 10. (Color online) The change δ(−IpCOHP) of the inverted integrated projected crystal orbital Hamilton population when a 10% C_{44} [110]-oriented shearing strain is applied, versus the group number of their corresponding metals, of the pyrite-type transition-metal pernitrides. Pugh's ratio (k) is shown for comparison. The pernitrides corresponding to metals from the 3*d* row are represented by black circles. Blue squares represent pyrite-type TcN_2, and red triangles represent pyrite-type PtN_2 for comparison. Mechanically unstable phases are omitted causing breaks in the lines, which are a guide to the eye. Notice the anticorrelation between δ(−IpCOHP) of *M*-*M* and k.

Furthermore, a case worth mentioning is PtN_2. Its value of δ(−IpCOHP) of Pt-Pt, −11.2 meV, being negative is different from all other phases. Its value of k (0.68), which is not much larger than that of the other hard phases, is indicative enough of its brittle nature. Its value of G (181.1 GPa), on the other hand, is much larger than the following candidates: MnN_2 (130.4 GPa) and CoN_2 (131.1 GPa). This negative δ(−IpCOHP) value may shed light on its extraordinarily high G, k, and H_V values relative to all the other nitrides in our study. It is understood as follows. When the shearing strain causes some of the metal atoms, originally far away, to get closer, the Pt-Pt bond becomes weaker; the system total energy climbs up the strain-dependent curve very quickly, yielding large values of related elastic constants and, furthermore, large values of shear related mechanical properties k, G, and H_V. As a reminder, PtN_2 has the largest values of H_V (23.5 GPa) in this paper. In addition to the negative δ(−IpCOHP) value, in Table V the −IpCOHP value of Pt-Pt

in an unstrained conventional cell of PtN_2 is −191.3 meV, also very negative. Taking both of them into consideration, we are more certain of the antibonding nature of the Pt-Pt bond. It discourages the free travel of electrons among the Pt atom network, demonstrating the semiconducting behavior of PtN_2. This is certainly not to say that semiconductors or insulators are generally harder. However, in a certain class of materials, in this case the transition-metal pyrite-type pernitrides and possibly other similar compositions and structures, if we find a few semiconducting or insulating phases out of the many metallic phases, they are much more likely to be harder.

IV. CONCLUSION

We carried out a systematic analysis on transition-metal pernitrides (MN_2) in the pyrite structure with spin-polarized DFT. Below is a summary of what we did and found.

(a) The cohesive energy of these phases at their equilibrium volume was compared with that of their counterparts in fluorite structure, and pyrite-type phases were concluded to be mostly more energetically favorable. Besides, most of fluorite-type phases are mechanically unstable as well.

(b) The structural parameters, including lattice constant, internal parameter, and bond lengths between different atoms were provided. Among these trends, we noticed d(N-N) did not follow the trends of the others, and explanations were provided later on.

(c) We calculated elastic constants C_{11}, C_{12}, and C_{44} for each phase and derived polycrystalline mechanical properties (B, G, k, H_V) from them. Among these three, hardest phases show up in the 3d transition-metal row, highlighting MnN_2 (H_V = 19.9 GPa), CoN_2 (16.5 GPa), and NiN_2 (15.7 GPa). Overall, pyrite-type 5d metal pernitride PtN_2 has the largest value of H_V (23.5 GPa).

(d) The shortening of the N-N bond is ascribed to the decrease in charge transfer (q_{trans}) from M to N when one monitors the pernitrides from early to late transition-metal elements. Charge transfer exerts its effect majorly by providing Coulomb repulsion between the pairing N atoms. A correlation with B is suggested. We note that for pyrite-type transition-metal pernitrides, charge transfer or ionicity is not a major controlling factor of a material's shear related mechanical properties.

(e) The trend and transition of total electronic DOS of the 10 3d transition-metal pernitrides was observed, and we again correlated elastic constant C_{44}, an indicator of mechanical stability and hardness, with DOS at E_F, an indicator of metallicity. We further notice that the optimal VEC for shear related mechanical properties varies for different structures and could be more than one for a specific structure.

(f) We found an anticorrelation between M-M δ(−IpCOHP) and Pugh's ratio (k) and weaker anticorrelations with G and H_V. This is a direct connection between a specific bond and polycrystalline mechanical properties.

ACKNOWLEDGMENTS

We thank the Ohio Supercomputer Center (OSC) for computing resources. We thank the National Science Foundation CMMI 1234777, CNS 0855134, DMR CMMI 0928440, and CMMI 0933069 for funding this work.

[1] E. Gregoryanz, C. Sanloup, M. Somayazulu, J. Badro, G. Fiquet, H. K. Mao, and R. J. Hemley, Nat. Mater. **3**, 294 (2004).
[2] R. Yu and X. F. Zhang, Appl. Phys. Lett. **86**, 121913 (2005).
[3] C. Z. Fan, L. L. Sun, Y. X. Wang, Z. J. Wei, R. P. Liu, S. Y. Zeng, and W. K. Wang, Chinese Phys. Lett. **22**, 2637 (2005).
[4] S. K. R. Patil, S. V. Khare, B. R. Tuttle, J. K. Bording, and S. Kodambaka, Phys. Rev. B **73**, 104118 (2006).
[5] A. F. Young, J. A. Montoya, C. Sanloup, M. Lazzeri, E. Gregoryanz, and S. Scandolo, Phys. Rev. B **73**, 153102 (2006).
[6] J. C. Crowhurst, A. F. Goncharov, B. Sadigh, C. L. Evans, P. G. Morrall, J. L. Ferreira, and A. J. Nelson, Science **311**, 1275 (2006).
[7] R. Yu, Q. Zhan, and X. F. Zhang, Appl. Phys. Lett. **88**, 051913 (2006).
[8] H. Gou, L. Hou, J. Zhang, G. Sun, L. Gao, and F. Gao, Appl. Phys. Lett. **89**, 141910 (2006).
[9] Bilbao Crystallographic Server—Wyckoff Positions of Group 205 (Pa-3), http://www.cryst.ehu.es/cgi-bin/cryst/programs/nph-wp-list?gnum = 205 (accessed May 3, 2014).
[10] A. F. Young, C. Sanloup, E. Gregoryanz, S. Scandolo, R. J. Hemley, and H. K. Mao, Phys. Rev. Lett. **96**, 155501 (2006).
[11] J. C. Crowhurst, A. F. Goncharov, B. Sadigh, J. M. Zaug, D. Aberg, Y. Meng, and V. B. Prakapenka, J. Mater. Res. **23**, 1 (2008).
[12] K. Niwa, D. Dzivenko, K. Suzuki, R. Riedel, I. Troyan, M. Eremets, and M. Hasegawa, Inorg. Chem. **53**, 697 (2014).
[13] D. Aberg, B. Sadigh, J. Crowhurst, and A. F. Goncharov, Phys. Rev. Lett. **100**, 095501 (2008).
[14] J. A. Montoya, A. D. Hernandez, C. Sanloup, E. Gregoryanz, and S. Scandolo, Appl. Phys. Lett. **90**, 011909 (2007).
[15] R. Yu, Q. Zhan, and L. C. De Jonghe, Angew. Chem. Int. Ed. **46**, 1136 (2007).
[16] Z. W. Chen, X. J. Guo, Z. Y. Liu, M. Z. Ma, Q. Jing, G. Li, X. Y. Zhang, L. X. Li, Q. Wang, Y. J. Tian, and R. P. Liu, Phys. Rev. B **75**, 054103 (2007).
[17] Z. J. Wu, X. F. Hao, X. J. Liu, and J. Meng, Phys. Rev. B **75**, 054115 (2007).
[18] Z. J. Wu, E. J. Zhao, H. P. Xiang, X. F. Hao, X. J. Liu, and J. Meng, Phys. Rev. B **76**, 054115 (2007).
[19] D. Aberg, P. Erhart, J. Crowhurst, J. M. Zaug, A. F. Goncharov, and B. Sadigh, Phys. Rev. B **82**, 104116 (2010).
[20] E. R. Hernandez and E. Canadell, J. Mater. Chem. **18**, 2090 (2008).
[21] M. Wessel and R. Dronskowski, JACS **132**, 2421 (2010).
[22] J. von Appen, M. W. Lumey, and R. Dronskowski, Angew. Chem. Int. Ed. **45**, 4365 (2006).
[23] R. Dronskowski and P. E. Blochl, J. Phys. Chem. **97**, 8617 (1993).
[24] G. Soto, Comput. Mater. Sci. **61**, 1 (2012).

[25] S. K. R. Patil, N. S. Mangale, S. V. Khare, and S. Marsillac, Thin Solid Films **517**, 824 (2008).

[26] W. Chen, J. S. Tse, and J. Z. Jiang, Solid State Commun. **150**, 181 (2010).

[27] V. L. Deringer, A. L. Tchougreeff and R. Dronskowski, J. Phys. Chem. A **115**, 5461 (2011).

[28] S. Maintz, V. L. Deringer, A. L. Tchougreeff, and R. Dronskowski, J. Comput. Chem. **34**, 2557 (2013).

[29] Crystal Orbital Hamilton Populations: The Official Reference Page, http://cohp.de/ (accessed May 3, 2014).

[30] H. Holleck, J. Vac. Sci. Technol. A **4**, 2661 (1986).

[31] H. W. Hugosson, U. Jansson, B. Johansson, and O. Eriksson, Science **293**, 2434 (2001).

[32] D. G. Sangiovanni, L. Hultman, and V. Chirita, Acta Mater. **59**, 2121 (2011).

[33] D. G. Sangiovanni, V. Chirita, and L. Hultman, Thin Solid Films **520**, 4080 (2012).

[34] H. O. Pierson, *Handbook of Refractory Carbides & Nitrides: Properties, Characteristics, Processing and Applications* (Elsevier Science, Amsterdam, 1996), Chap. 3, Sec. 7 and Chap. 10, Sec. 5.

[35] G. Kresse and J. Furthmuller, Phys. Rev. B **54**, 11169 (1996).

[36] G. Kresse and J. Furthmuller, Comput. Mater. Sci. **6**, 15 (1996).

[37] G. Kresse and J. Hafner, Phys. Rev. B **49**, 14251 (1994).

[38] G. Kresse and J. Hafner, Phys. Rev. B **47**, 558 (1993).

[39] P. Hohenberg and W. Kohn, Phys. Rev. **136**, B864 (1964).

[40] W. Kohn and L. J. Sham, Phys. Rev. **140**, A1133 (1965).

[41] P. E. Blöchl, Phys. Rev. B **50**, 17953 (1994).

[42] G. Kresse and D. Joubert, Phys. Rev. B **59**, 1758 (1999).

[43] J. P. Perdew, J. A. Chevary, S. H. Vosko, K. A. Jackson, M. R. Pederson, D. J. Singh, and C. Fiolhais, Phys. Rev. B **46**, 6671 (1992).

[44] J. P. Perdew, J. A. Chevary, S. H. Vosko, K. A. Jackson, M. R. Pederson, D. J. Singh, and C. Fiolhais, Phys. Rev. B **48**, 4978 (1993).

[45] The PAW and US-PP database, http://cms.mpi.univie.ac.at/vasp-workshop/slides/pseudoppdatabase.pdf (accessed May 3, 2014).

[46] H. J. Monkhorst and J. D. Pack, Phys. Rev. B **13**, 5188 (1976).

[47] J. D. Pack and H. J. Monkhorst, Phys. Rev. B **16**, 1748 (1977).

[48] F. Birch, Phys. Rev. **71**, 809 (1947).

[49] F. Birch, Journal of Geophysical Research **83**, 1257 (1978).

[50] E. J. Zhao, J. P. Wang, J. Meng, and Z. J. Wu, Comput. Mater. Sci. **47**, 1064 (2010).

[51] M. J. Mehl, J. E. Osburn, D. A. Papaconstantopoulos, and B. M. Klein, Phys. Rev. B **41**, 10311 (1990).

[52] J. F. Nye, *Physical Properties of Crystals: Their Representation by Tensors and Matrices* (Clarendon Press, Oxford, 1985).

[53] X. Q. Chen, H. Y. Niu, D. Z. Li, and Y. Y. Li, Intermetallics **19**, 1275 (2011).

[54] Y. J. Tian, B. Xu, and Z. S. Zhao, Int J Refract Met H **33**, 93 (2012).

[55] Z. T. Y. Liu, X. Zhou, D. Gall, and S. V. Khare, Comput. Mater. Sci. **84**, 365 (2014).

[56] Z. T. Y. Liu, X. Zhou, S. V. Khare, and D. Gall, J. Phys.-Condens. Matter **26**, 025404 (2014).

[57] X. Zhou, D. Gall, and S. V. Khare, J. Alloys Compd. **595**, 80 (2014).

[58] R. F. W. Bader, *Atoms in Molecules: a Quantum Theory* (Oxford University Press, New York, 1990).

[59] F. W. Bieglerkonig, R. F. W. Bader, and T. H. Tang, J. Comput. Chem. **3**, 317 (1982).

[60] Bader Charge Analysis, http://theory.cm.utexas.edu/bader/ (accessed May 3, 2014).

[61] G. Henkelman, A. Arnaldsson, and H. Jonsson, Comput. Mater. Sci. **36**, 354 (2006).

[62] E. Sanville, S. D. Kenny, R. Smith, and G. Henkelman, J. Comput. Chem. **28**, 899 (2007).

[63] W. Tang, E. Sanville, and G. Henkelman, J. Phys.-Condens. Matter **21**, 084204 (2009).

[64] Using the Bader analysis with the VASP code, http://theory.cm.utexas.edu/bader/vasp.php (accessed May 3, 2014).

[65] P. E. Blöchl, O. Jepsen, and O. K. Andersen, Phys. Rev. B **49**, 16223 (1994).

[66] R. Hoffmann, *Solids and Surfaces: A Chemist's View of Bonding in Extended Structures* (Wiley-VCH, Berlin, 1989).

[67] T. Hughbanks and R. Hoffmann, JACS **105**, 3528 (1983).

[68] C. Stampfl, W. Mannstadt, R. Asahi, and A. J. Freeman, Phys. Rev. B **63**, 155106 (2001).

[69] Y. M. Juan and E. Kaxiras, Phys. Rev. B **48**, 14944 (1993).

[70] D. G. Sangiovanni, V. Chirita and L. Hultman, Phys. Rev. B **81**, 104107 (2010).

[71] See Supplemental Material at http://link.aps.org/supplemental/10.1103/PhysRevB.90.134102 for DOS figures of IrN_2, AuN_2. DOS figures of Group 4 and Group 10 pernitrides are also available with a short discussion of the transition between metallic and nonmetallic phases.